# Supporting Information

## Solvent-Driven Self-Assembly and Polarized Emission in Nitrogen-Doped Graphene Quantum Dots

Subhro Kundu,[a] Abu Bakar Siddique,[a] Irvin Fernando Guzmán González,[a] Kevin Armando Rodríguez Mireles,[a] Maritza Iveth Pérez Valverde,[a] Nicolás Antonio Ulloa Castillo,[a] Madhusoodanan Reghunathan,[b] Domingo Ixcoatl García Gutiérrez,[b,c,] Eduardo Martínez Guerra,[d] and Mallar Ray [a]*

[a] School of Engineering and Sciences, Tecnológico de Monterrey, Monterrey, Nuevo León 64849, Mexico.

[b] Universidad Autónoma de Nuevo León, Centro de Innovación, Investigación y Desarrollo en Ingeniería y Tecnología, Apodaca, 66600, Nuevo León, México

[c] Universidad Autónoma de Nuevo León, Facultad de Ingeniería Mecánica y Eléctrica, San Nicolás de los Garza, 66455, Nuevo León, México

[d] Centro de Investigaciones en Materiales Avanzados, CIMAV Unidad Monterrey, Alianza Norte 202, Apodaca, Nuevo León, C.P. 66628, Mexico.

**Email:** mallar.ray@tec.mx

### Section 1: Details of photoinduced force microscopy

**Spatial resolution:** The Vista One PiFM system from Molecular Vista achieves spatial resolution in topography that is primarily determined by the tip's radius of curvature and the precision of the AFM scanner. As noted in the main text, the tip has a radius of curvature of 67 nm, while the scanner offers a precision of 100 pm RMS along the x, y, and z axes. The lateral (xy) resolution depends on both the tip geometry and the surface features of the sample. Since the GQDs and NGQDs were deposited on a flat substrate, lateral measurements were facilitated; by accounting for tip convolution, a close estimate of the actual particle size can be obtained. The height resolution is governed solely by the scanner's

precision, and the 100 pm RMS capability is sufficient to accurately measure features with heights below 10 nm in our samples.

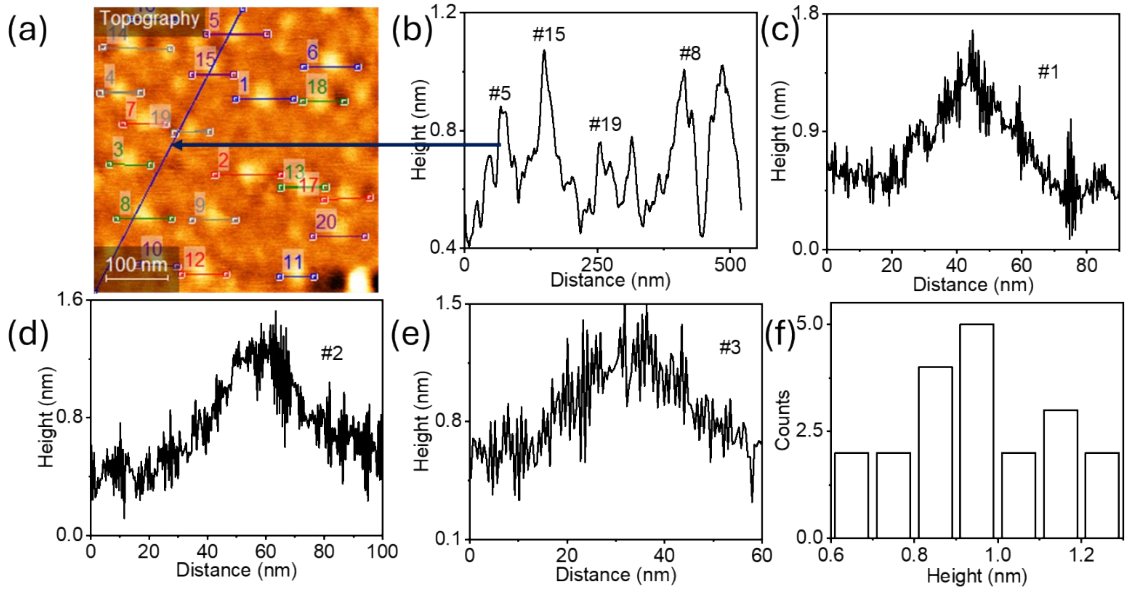


**Figure S1:** AFM analysis of the synthesized NGQD. (a) selected area AFM topography, (b) Wide scan line profile of the deposited NGQDs as shown by blue line in AFM micrograph containing particle #5, #15, #19, #8, (c-e) arbitrarily selected line profiles of the NGQDs, (f) height profile of the synthesized NGQDs,.

**Tip deconvolution:** The AFM tip used in this study had a radius of curvature of 67 nm. Because the average particle sizes were smaller than the tip radius, we applied the following equation to correct for the tip convolution effect.[1]

$$S = 2 \times \left( R \times D + \frac{D^2}{4} \right)^{1/2}$$

**Spectral Resolution:** The spectral resolution is 1 $cm^{-1}$, enabled by a high-performance tunable IR laser – specifically, a Quantum Cascade Laser (QCL) from Block Engineering, covering a spectral range of 744–1884 $cm^{-1}$. The Vista One PiFM system is accurately calibrated using well-established IR calibration standards, including polyethersulfone (PES), polymethyl methacrylate (PMMA), Nylon, as well as AFM calibration substrates composed of silicon and silicon oxide.

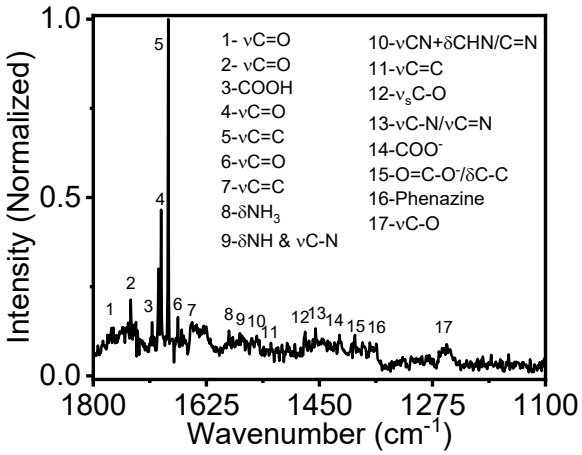


**Figure S2:** PiFIR spectra of the synthesized NGQDs.

**Table S1:** Correlation table for peaks, relative intensity, and position from PiF-IR of the NGQD from figure S2.

| Peak Number | PiFIR Wavenumber ($cm^{-1}$) | DFT Wavenumber ($cm^{-1}$) | Difference in Experiment and Theory ($cm^{-1}$) | Functional groups |
|---|---|---|---|---|
| 1. | 1770 | 1774 | -4 | νC=O[2] |
| 2. | 1742 | 1747 | -5 | νC=O[3] |
| 3. | 1709 | 1707 | 2 | COOH[4] |
| 4. | 1695 | - | | νC=O[5] |
| 5. | 1684 | 1679 | 5 | νC=C[6,7] |
| 6. | 1669 | 1672 | -3 | νC=O[8] |
| 7. | 1649 | 1646 | 3 | νC=C[3] |
| 8. | 1591-1588 | 1598 | -7 to -10 | $\delta NH_3$[9] |
| 9. | 1570-1567 | 1574 | -4 to -10 | δN-H & νC-N[10] |
| 10. | 1547-1545 | 1551 | -4 to -7 | νCN+δCHN/C=N[6,11] |
| 11. | 1525 | 1521 | 4 | νC=C[12] |
| 12 | 1472 | 1478 | 6 | $\nu_s$C-O[13] |
| 13. | 1456 | 1453 | 3 | C–N/C=N[5] |
| 14. | 1419 | 1420 | -1 | $COO^-$[14] |
| 15. | 1395 | 1400 | -5 | O=C-O-/δC-C[15,16] |
| 16. | 1354 | 1357 | -3 | C=N/phenazine[17] |
| 17. | 1251 | 1255 | -4 | νC-O[18] |

**Section 2: Details of FTIR analysis**

The ensemble-averaged FTIR spectrum [Figure 1(g)] reflects the distribution of chemical heterogeneity observed directly at the single-particle level by PiFM. Broad O–H and N–H stretching bands (~3250 $cm^{-1}$) alongside C–H stretching (~2930 $cm^{-1}$) indicate abundant hydroxyl, amine, and hydrocarbon

functionalities [19]. Distinct skeletal C=C vibrations (2160 and 1650 $cm^{-1}$) point to conjugated $sp^2$ carbon domains, while the coupled δN–H and νC≡N mode at 1535 $cm^{-1}$ suggests interactions between amine and nitrile groups [19]. Peaks between 1386–1350 $cm^{-1}$ correspond to C–N stretching and phenazine-like nitrogen species, and additional bands at 1438, 1295, 1180, and 1108 $cm^{-1}$ are attributed to various oxygen- and nitrogen-bearing groups, such as C–O, C–N, and epoxy or ether moieties [17,20 21–24]. These vibrational signatures corroborate the heterogeneous surface composition and functional group diversity that underpins the solubility and reactivity of N-GQDs. Importantly, the consistent identification of oxygen- and nitrogen-containing functional groups across both techniques underscores the robustness of the observed chemical diversity, reinforcing the role of these moieties in defining the optical and chemical properties of N-GQDs.

**Section 3: Additional optical characterization results**

**Excitation threshold ($\lambda_{th}$ / $E_{th}$.):** Determination of the excitation threshold separating wavelength-independent and wavelength-dependent emission regimes from intersection of linear fits in excitation emission plots shown in Figure S3.

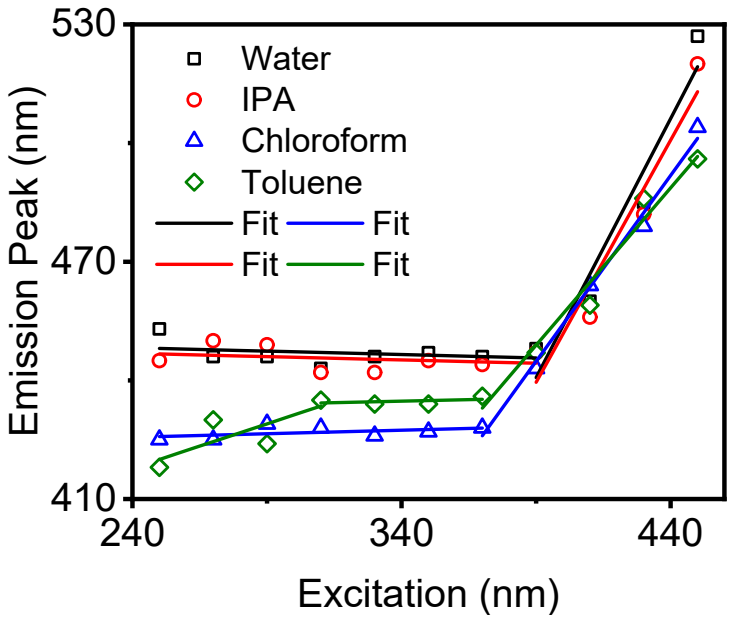


**Figure S3:** Excitation dependent emission spectra of the NGQDs in different solvents – water, IPA, chloroform, toluene. Scatter plots represent the experimental data, and the solid lines represent the linear fits to find out the $\lambda_{th}$ or $E_{th}$.

**Table S2: Triexponential fitting parameters of TRPL spectra of NGQDs in different solvents.**

| Solvent | $\alpha_1$ | $\tau_1$(ns) | $\alpha_2$ | $\tau_2$(ns) | $\alpha_3$ | $\tau_3$(ns) | $\tau_{avg}$(ns) | $R^2$ |
|---|---|---|---|---|---|---|---|---|
| Water | 677.9 | 11.4 | 692 | 16.8 | 687 | 17.5 | 15.8 | 0.99 |
| IPA | 1181 | 8.9 | 1168 | 9.3 | 639 | 12.6 | 10.1 | 0.99 |
| Chloroform | 2250 | 6.7 | 2867 | 6.7 | 5 | 77.1 | 7.4 | 0.99 |
| Toluene | 2156 | 6.9 | 2363 | 6.9 | 7.8 | 41.3 | 7.2 | 0.99 |

**Complete set of angle-resolved PL emissions in different solvents**

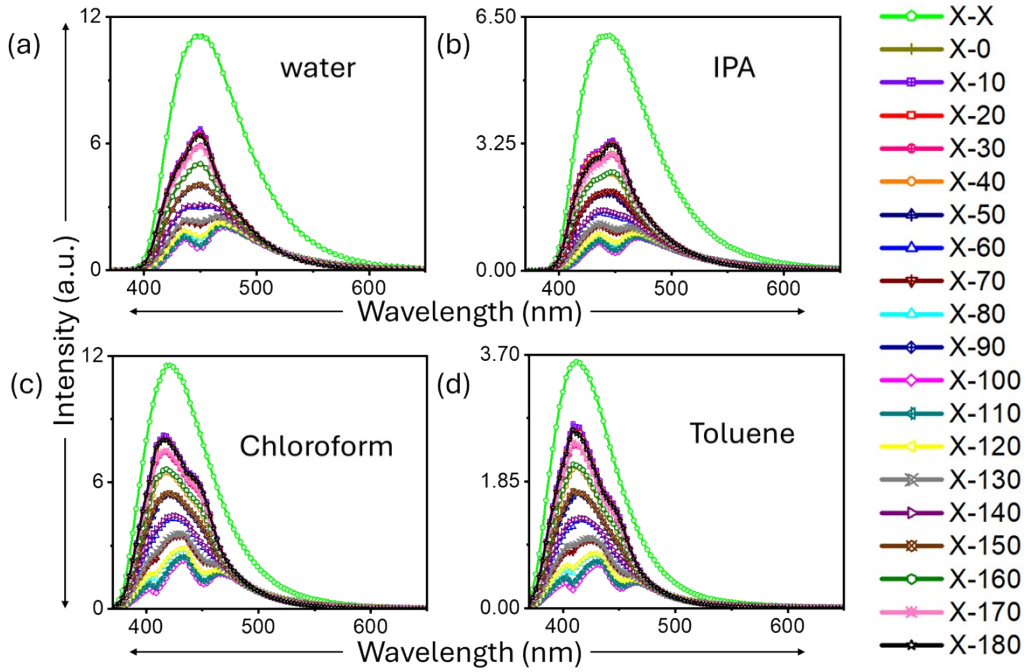


**Figure S4:** The complete set of PL spectra of NGQDs in different solvents at different analyzer angles configuration (as indicated in the legend) for (a) water, (b) IPA, (c) chloroform, and (d) toluene.

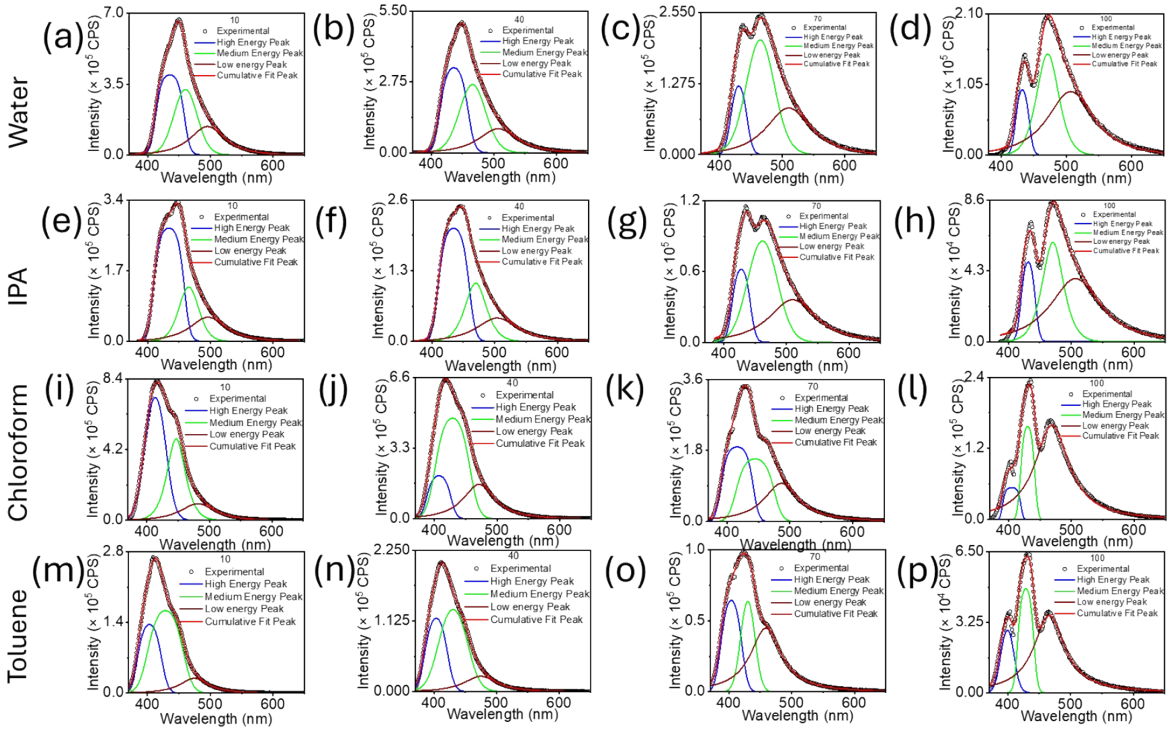


**Figure S5:** The complete set of deconvoluted PL spectra of NGQDs in different solvents and different analyzer angles. Row wise solvents – top to bottom: water, IPA, chloroform, and toluene, and from left to right: analyzer angles at 10°, 40°, 70°, 100°.

After deconvolution the area of the individual peaks or the integrated intensity of the individual peaks were recorded with respect to the analyzer angle. Subsequently, scatter plots were made with the integrated intensity versus the respective analyzer angles, and the plots were fitted with the expression of Malus' Law: $I = I_0 \cos^2(\theta - \theta_0)$

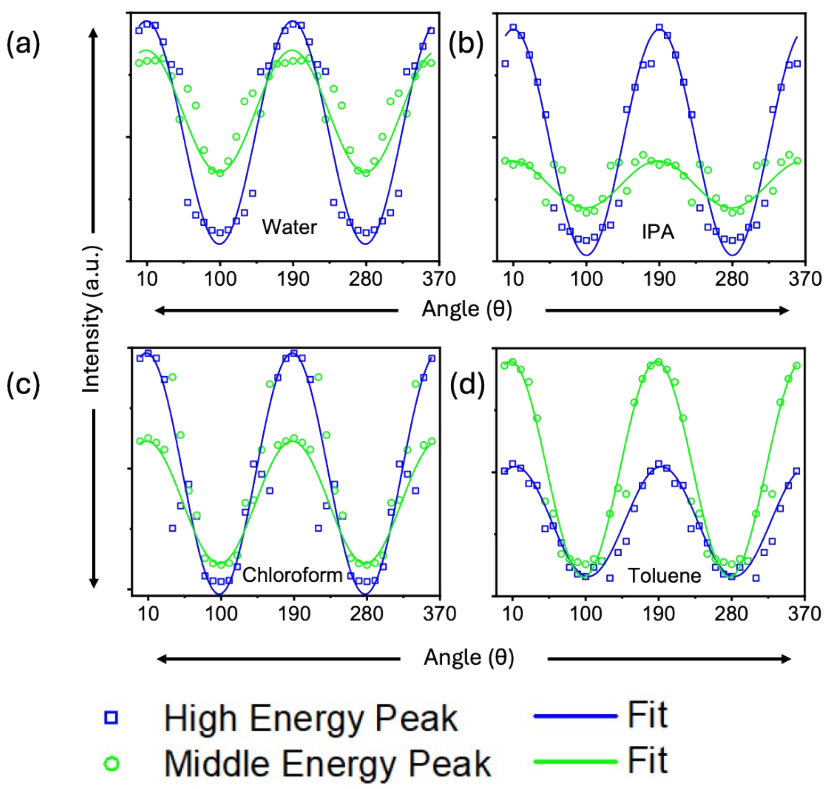


**Figure S6:** Angular dependent periodic variation of integrated PL intensity of the high energy and mid energy peaks of NGQDs in different solvents: (a) water, (b) IPA, (c) Chloroform, (d) Toluene.

**Section 4: Zeta Potential analysis**

Zeta potential measurements of the NGQDs were performed using a Zetasizer Nano ZS (Malvern Instruments, UK) operating in electrophoretic light scattering mode. NGQD dispersions were prepared at a concentration of 0.1 mg $mL^{-1}$ in the four different solvents: DI water, IPA, chloroform, and toluene. For aqueous measurements, the pH of the dispersion was recorded, whereas for non-aqueous solvents values were not reported, as pH is not defined in these media, measurements were interpreted considering the dielectric constant and viscosity of the respective solvents. All measurements were conducted at room temperature (~25 °C). Disposable folded capillary cells were used for water and IPA, while quartz cuvettes were used for chloroform and toluene to ensure solvent compatibility. Each sample was analyzed in triplicate to ensure reproducibility.

**Section 5: Wood's anomaly and polarizer response**

In the emission spectra measured with the FLS1000, sharp intensity dips can appear at specific wavelengths (e.g., around 398 nm and 470 nm) due to Wood's anomalies, which are abrupt decreases in diffraction grating efficiency when the polarization component of light is parallel to the grating grooves. These anomalies are artefacts of the instrument's optical components rather than intrinsic features of the sample. The Edinburgh Instruments system removes such distortions through an emission correction factor, which is determined by comparing the spectrometer's measured response to that of NPL- or NIST-traceable calibration sources with known spectral outputs. By scaling the measured data with this wavelength-dependent correction factor, the influence of grating efficiency variations, PMT quantum efficiency changes, and optical transmission losses is eliminated. As a result, Wood's anomalies are suppressed in the corrected spectrum, ensuring that the recorded emission profile accurately represents the true photoluminescence of the sample.[25]

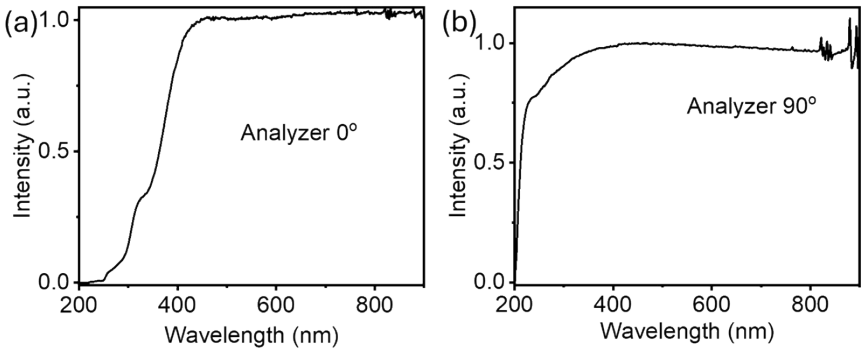


**Figure S7:** Spectral response of the analyzer for different angles. (a) Analyzer response in calcite at an angle 0º, (b) analyzer performance in $BBO_2$ at an angle 90º. (Data provided by Edinburgh Instruments)

**Section 6: Solvent polarity, zeta potential and the variation in DOP**

**Table S3: Dipole moment, zeta potentials of solvents and corresponding DOP of PL emission**

| Solvent | Dipole moment (Debye) | Zeta Potential (mV) | DOP High Energy peak | DOP Medium energy peak | Angle of Dipole ($\theta_0$) High Energy peak | Angle of Dipole ($\theta_0$) Medium Energy peak |
|---|---|---|---|---|---|---|
| Water | 3 | -16.6 | 0.866 | 0.406 | 9.08 | 8.65 |
| IPA | 1.66 | -13.9 | 0.94 | 0.305 | 10.09 | 8.29 |
| Chloroform | 1.15 | 42.6 | 0.987 | 0.701 | 7.66 | 7.69 |
| Toluene | 0.375-0.43 | 85 | 0.735 | 0.84 | 13.21 | 7.24 |

**Reference**


1 A. Engel, C.-A. Schoenenberger and D. J. Müller, *Curr Opin Struct Biol*, 1997, **7**, 279–284.

2 J. A. Prince, S. Bhuvana, V. Anbharasi, N. Ayyanar, K. V. K. Boodhoo and G. Singh, *Water Res*, 2016, **103**, 311–318.

3 S. Pei, Q. Wei, K. Huang, H.-M. Cheng and W. Ren, *Nat Commun*, 2018, **9**, 145.

4 K. Pan, Y. Fan, T. Leng, J. Li, Z. Xin, J. Zhang, L. Hao, J. Gallop, K. S. Novoselov and Z. Hu, *Nat Commun*, 2018, **9**, 5197.

5 F. Rigodanza, M. Burian, F. Arcudi, L. Đorđević, H. Amenitsch and M. Prato, *Nat Commun*, 2021, **12**, 2640.

6 V. Ţucureanu, A. Matei and A. M. Avram, *Taylor and Francis Ltd.*, 2016, preprint, DOI: 10.1080/10408347.2016.1157013.

7 Y. Yamada, M. Kawai, H. Yorimitsu, S. Otsuka, M. Takanashi and S. Sato, *ACS Appl Mater Interfaces*, 2018, **10**, 40710–40739.

8 G. Zhan, L. Hu, H. Li, J. Dai, L. Zhao, Q. Zheng, X. Zou, Y. Shi, J. Wang, W. Hou, Y. Yao and L. Zhang, *Nat Commun*, 2024, **15**, 5918.

9 J.-Y. Fang, Q.-Z. Zheng, Y.-Y. Lou, K.-M. Zhao, S.-N. Hu, G. Li, O. Akdim, X.-Y. Huang and S.-G. Sun, *Nat Commun*, 2022, **13**, 7899.

10 F. S. Ruggeri, G. Longo, S. Faggiano, E. Lipiec, A. Pastore and G. Dietler, *Nat Commun*, 2015, **6**, 7831.

11 R. Shi, L. Liu, Y. Lu, C. Wang, Y. Li, L. Li, Z. Yan and J. Chen, *Nat Commun*, 2020, **11**, 178.

12 P. K. Srivastava, P. Yadav and S. Ghosh, *Nanoscale*, 2016, **8**, 15702–15711.

13 X. He, J. M. Larson, H. A. Bechtel and R. Kostecki, *Nat Commun*, 2022, **13**, 1398.

14 M. Wang, R. Wang, H. Yao, Z. Wang and S. Zheng, *RSC Adv*, 2016, **6**, 63365–63372.

15 Z. Jovanović, Ž. Mravik, D. Bajuk-Bogdanović, S. Jovanović, S. Marković, M. Vujković, J. Kovač, D. Vengust, S. Uskoković-Marković and I. Holclajtner-Antunović, *Carbon N Y*, 2020, **156**, 166–178.

16 J. M. Wang, Q. Y. Zhu, J. H. Lee, T. G. Woo, Y. X. Zhang, W.-D. Jang and T. K. Kim, *Nat Commun*, 2023, **14**, 3808.

17 J. Guo, Y. Xu, S. Jin, L. Chen, T. Kaji, Y. Honsho, M. A. Addicoat, J. Kim, A. Saeki, H. Ihee, S. Seki, S. Irle, M. Hiramoto, J. Gao and D. Jiang, *Nat Commun*, 2013, **4**, 2736.

18 A. Ngqalakwezi, D. Nkazi, G. Seifert and T. Ntho, *Catal Today*, 2020, **358**, 338–344.

19 S. Mallakpour and E. Khadem, *Int J Biol Macromol*, 2018, **120**, 1451–1460.

20 S. Kumar, P. Kumar, A. Deb, D. Maiti and S. L. Jain, *Carbon N Y*, 2016, **100**, 632–640.

21 W. Chen, K. A. Tarach, X. Yi, Z. Liu, X. Tang, K. Góra-Marek and A. Zheng, *Nat Commun*, 2022, **13**, 7106.

22 D. Wu, K. Luo, S. Du and X. Hu, *J Power Sources*, 2018, **398**, 99–105.

23 D. Du, P. Li and J. Ouyang, *ACS Appl Mater Interfaces*, 2015, **7**, 26952–26958.

24 H. Khojasteh, M. Salavati-Niasari, H. Safajou and H. Safardoust-Hojaghan, *Diam Relat Mater*, 2017, **79**, 133–144.

25 R. W. Wood, *Physical Review*, 1935, **48**, 928–936.